

Low-latency gravitational wave alert products and their performance in anticipation of the fourth LIGO-Virgo-KAGRA observing run

SUSHANT SHARMA CHAUDHARY*¹ AND ANDREW TOIVONEN†²

THESE AUTHORS CONTRIBUTED EQUALLY TO THIS WORK

GAURAV WARATKAR³, GEOFFREY MO⁴, PATRICK BROCKILL⁵, DEEP CHATTERJEE⁴, MICHAEL W. COUGHLIN²,
REED ESSICK^{6,7,8}, SHAON GHOSH⁹, SOICHIRO MORISAKI¹⁰, PRATYUSAVA BARAL⁵, AMANDA BAYLOR⁵

NARESH ADHIKARI⁵, SARAH ANTIER¹¹, PATRICK BRADY⁵, GARETH CABOURN DAVIES¹², TITO DAL CANTON¹³,
MARCO CAVAGLIA¹, JOLIEN CREIGHTON¹⁴, SUNIL CHOUDAHRY^{15,16}, YU-KUANG CHU⁵, PATRICK CLEARWATER^{15,16},
LUKE DAVIS^{15,16}, THOMAS DENT¹⁷, MARCO DRAGO¹⁸, BECCA EWING^{19,20}, PATRICK GODWIN²¹,
WEICHANGFENG GUO^{15,16}, CHAD HANNA^{19,20,22,23}, RACHEL HUXFORD^{19,20}, IAN HARRY¹², ERIK KATSAVOUNIDIS⁴,
MANOJ KOVALAM^{15,16}, ALVIN K.Y. LI²¹, RYAN MAGEE²¹, ETHAN MARX⁴, DUNCAN MEACHER⁵,
CODY MESSICK⁵, XAN MORICE-ATKINSON¹², ALEXANDER PACE²⁴, ROBERTO DE PIETRI^{25,26},
BRANDON PIOTRZKOWSKI⁵, SOUMEN ROY^{27,28}, SURABHI SACHDEV^{5,29}, LEO P. SINGER^{30,31}, DIVYA SINGH^{19,20},
MAREK SZCZEPANCZYK³², DANIEL TANG^{15,16}, MAX TREVOR³³, LEO TSUKADA^{19,20}, VERÓNICA VILLA-ORTEGA¹⁷,
LINQING WEN^{15,16} AND DANIEL WYSOCKI⁵

¹*Institute of Multi-messenger Astrophysics and Cosmology, Missouri University of Science and Technology, Physics Building, 1315 N. Pine St., Rolla, MO 65409, USA*

²*School of Physics and Astronomy, University of Minnesota, Minneapolis, Minnesota 55455, USA*

³*Department of Physics, IIT Bombay, Powai, Mumbai, 400076, India*

⁴*LIGO Laboratory and Kavli Institute for Astrophysics and Space Research, Massachusetts Institute of Technology, 185 Albany Street, Cambridge, Massachusetts 02139, USA*

⁵*Leonard E. Parker Center for Gravitation, Cosmology, and Astrophysics, University of Wisconsin-Milwaukee, Milwaukee, WI 53201, USA*

⁶*Canadian Institute for Theoretical Astrophysics, University of Toronto, Toronto, ON M5S 3H8*

⁷*Department of Physics, University of Toronto, Toronto, ON M5S 1A7*

⁸*David A. Dunlap Department of Astronomy, University of Toronto, Toronto, ON M5S 3H4*

⁹*Montclair State University, 1 Normal Ave. Montclair, NJ 07043*

¹⁰*Institute for Cosmic Ray Research, The University of Tokyo, 5-1-5 Kashiwanoha, Kashiwa, Chiba 277-8582, Japan*

¹¹*Artemis, Observatoire de la Côte d'Azur, Université Côte d'Azur, Boulevard de l'Observatoire, 06304 Nice, France*

¹²*University of Portsmouth, Portsmouth, PO1 3FX, United Kingdom*

¹³*Université Paris-Saclay, CNRS/IN2P3, IJCLab, 91405 Orsay, France*

¹⁴*University of Wisconsin, Milwaukee, WI 53211, USA*

¹⁵*Australian Research Council Centre of Excellence for Gravitational Wave Discovery (OzGrav), Australia*

¹⁶*Department of Physics, University of Western Australia, Crawley WA 6009, Australia*

¹⁷*IGFAE, Universidad de Santiago de Compostela, E-15782 Spain*

¹⁸*Università di Roma La Sapienza, I-00133 Roma, Italy and INFN, Sezione di Roma, I-00133 Roma, Italy*

¹⁹*Department of Physics, The Pennsylvania State University, University Park, PA 16802, USA*

²⁰*Institute for Gravitation and the Cosmos, The Pennsylvania State University, University Park, PA 16802, USA*

²¹*LIGO Laboratory, California Institute of Technology, Pasadena, CA 91125, USA*

²²*Department of Astronomy and Astrophysics, The Pennsylvania State University, University Park, PA 16802, USA*

²³*Institute for Computational and Data Sciences, The Pennsylvania State University, University Park, PA 16802, USA*

²⁴*Department of Physics, Pennsylvania State University, University Park, PA 16802, USA*

²⁵*Dipartimento di Scienze Matematiche, Fisiche e Informatiche, Università di Parma, Parco Area delle Scienze 7/A, I-43124 Parma, Italy*

²⁶*INFN, Sezione di Milano Bicocca, Gruppo Collegato di Parma, I-43124 Parma, Italy*

*sscwrk@mst.edu

†toivo032@umn.edu

²⁷*Nikhef, Science Park 105, 1098 XG Amsterdam, The Netherlands*

²⁸*Institute for Gravitational and Subatomic Physics (GRASP), Utrecht University, Princetonplein 1, 3584 CC Utrecht, The Netherlands*

²⁹*School of Physics, Georgia Institute of Technology, Atlanta, GA 30332, USA*

³⁰*Astrophysics Science Division, NASA Goddard Space Flight Center, Code 661, Greenbelt, MD 20771, USA*

³¹*Joint Space-Science Institute, University of Maryland, College Park, MD 20742, USA*

³²*Department of Physics, University of Florida, Gainesville, FL 32611-8440, USA*

³³*University of Maryland, College Park, MD 20742, USA*

ABSTRACT

Multi-messenger searches for binary neutron star (BNS) and neutron star-black hole (NSBH) mergers are currently one of the most exciting areas of astronomy. The search for joint electromagnetic and neutrino counterparts to gravitational wave (GW)s has resumed with Advanced LIGO (aLIGO)’s, Advanced Virgo (AdVirgo)’s and KAGRA’s fourth observing run (O4). To support this effort, public semi-automated data products are sent in near real-time and include localization and source properties to guide complementary observations. Subsequent refinements, as and when available, are also relayed as updates. In preparation for O4, we have conducted a study using a simulated population of compact binaries and a Mock Data Challenge (MDC) in the form of a real-time replay to optimize and profile the software infrastructure and scientific deliverables. End-to-end performance was tested, including data ingestion, running online search pipelines, performing annotations, and issuing alerts to the astrophysics community. In this paper, we present an overview of the low-latency infrastructure as well as an overview of the performance of the data products to be released during O4 based on a MDC. We report on expected median latencies for the preliminary alert of full bandwidth searches (29.5 s) and for the creation of early warning triggers (-3.1 s), and show consistency and accuracy of released data products using the MDC. This paper provides a performance overview for LVK low-latency alert structure and data products using the MDC in anticipation of O4.

Keywords: gravitational waves, gravitational wave astronomy

1. INTRODUCTION

O4 is underway and began on May 24, 2023¹. This run follows a series of observing runs, which have reported the detection of the first binary black hole (BBH) in aLIGO’s first observing run (O1) (Abbott et al. 2016), the detection of the first BNS merger (Abbott et al. 2017a) and associated electromagnetic counterparts AT2017gfo (Coulter et al. 2017; Smartt et al. 2017; Abbott et al. 2017b) and GRB170817A (Goldstein et al. 2017; Savchenko et al. 2017; Abbott et al. 2017c) in the aLIGO’s and AdVirgo’s second observing run (O2), and NSBH (Abbott et al. 2021a) in the aLIGO’s and AdVirgo’s third observing run (O3). Focusing on neutron star (NS) mergers, there are a variety of science cases for their multi-messenger counterpart searches and detections, including measurements of the NS equation of state (EoS) (Bauswein et al. 2017; Margalit & Metzger 2017; Coughlin et al. 2019a, 2018, 2019b; Annala et al. 2018; Most et al. 2018; Radice et al. 2018; Lai et al. 2019; Dietrich et al. 2020; Huth et al. 2022), the

Hubble constant (Coughlin et al. 2020a,b; Abbott et al. 2017; Hotokezaka et al. 2018; Dietrich et al. 2020), and *r*-process nucleosynthesis (Chornock et al. 2017; Coulter et al. 2017; Cowperthwaite et al. 2017; Pian et al. 2017; Rosswog et al. 2017; Smartt et al. 2017; Watson et al. 2019; Kasliwal et al. 2019).

The LIGO-Virgo-KAGRA (LVK)’s real time alert infrastructure depends on several components. Broadly this includes low-latency data calibration and transfer, running of modeled and unmodeled online searches (see Section 2.1 for a brief description), and maintaining the state of events in GRAVitational-wave Candidate Event DataBase (GraceDB) following the discovery. In addition to GraceDB,² which serves as both the database and as an internal and external web view, the alert infrastructure includes `igwn-alert`,³ an internal messaging system to communicate the state of events, and `gwcelery`,⁴ a task queue, to cluster, annotate, and orchestrate the

¹ <https://observing.docs.ligo.org/plan>

² <https://gracedb.ligo.org/>

³ <https://igwn-alert.readthedocs.io>

⁴ <https://git.ligo.org/emfollow/gwcelery>

⁵ <https://rtd.igwn.org/projects/gwcelery/en/latest/>

events, as well as publish public alerts⁶ for the community to subscribe to. Figure 1 shows the task flow of the Low-Latency Alert Infrastructure (LLAI) for candidate events. The current LLAI is a significantly upgraded version of the infrastructure used earlier, described in LV 2019, and used in the more recently reported early-warning system, reported in Magee et al. 2021. The LVK Alert User Guide⁷ constitutes a living document where information and updates about this system are regularly communicated to the broader community.

To prepare for O4 and demonstrate performance across a variety of software and alert system improvements, we carried out a Mock Data Challenge (MDC). This MDC constitutes a testing environment for the LLAI to prepare for O4, producing repeated sets of 40 days of data from O3, with associated simulations of compact binary coalescences (CBCs) to stress test the system. While the rates of simulated events (see Section 4 for a description of the data set) were much higher than that expected for O4, this high rate was designed to test the various components of searches, the alert system and the scientific deliverables before heading into O4; these include, for example, tests of the detection efficiency of online real time low-latency searches, the rapid estimation of the binary system properties, and their associated sky localizations.

In this paper, we describe the details of the alert system for O4 and its performance based on this MDC. In addition, we provide an overview of the detection performance of real time searches, along with the consistency and accuracy of alert data products. Section 2 provides an overview of the LLAI and the scientific data products reported, while Section 3 describes the properties of the MDC, including the motivations for the choices made. Section 4 reports the properties of the LLAI as of the beginning of O4, as measured by the MDC, and Section 5 describes the conclusions and prospects for future development.

2. OVERVIEW OF ALERT SYSTEM AND SCIENTIFIC PRODUCTS

2.1. Searches

Low-latency GW searches consist of two categories: “modeled” CBC and “unmodeled” (Burst) searches. Modeled CBC searches target BNS, NSBH, or BBH (LVK 2021a); unmodeled searches look for signals with generic morphologies from a wide variety of astrophysical sources like core-collapse of massive stars, magne-

tar star-quakes, and other sources, in addition to compact binary mergers (LVK 2021b,c). For the purpose of this analysis, we focus on CBC searches, but also report Burst latencies. CBC searches can be categorized as early warning, referring to pre-merger searches, or full bandwidth, referring to post-merger, based on how the search truncates their templates. Each search produces candidate GW triggers and assigns them ranking statistic values and false alarm rates (FARs); the FAR for a trigger in a given search pipeline is defined as the expected rate of triggers due to detector noise, in that pipeline, with equal or higher ranking. Each search pipeline has different and independent methods of generating and ranking triggers and estimating the noise background and thus the FAR; for details see Messick et al. (2017); Aubin et al. (2021); Hooper et al. (2012); Luan et al. (2012); Usman et al. (2016); Dal Canton et al. (2021); Piotrkowski (2022). In addition, the probability of astrophysical origin, p_{astro} , for a trigger is calculated for CBC searches, which is described in detail in Section 2.3. In the following, we briefly describe key aspects of each pipeline participating in low-latency searches.

2.1.1. *GstLAL*

GStreamer LIGO Scientific Collaboration Algorithm Library (GstLAL) is a stream-based matched filtering algorithm capable of detecting GW signals within seconds of their arrival on Earth (Messick et al. 2017; Tsukada et al. 2023; Ewing et al. 2023). GstLAL uses a template bank of $\sim 10^6$ CBC waveforms in order to filter the full BNS, NSBH, and BBH regions of the parameter space (Sakon et al. 2022). The template bank is divided into $\sim 10^3$ bins of time-sliced singular value decomposition (SVD) waveforms according to the Low Latency Online Inspiral Detection (LLOID) method (Cannon et al. 2012). These waveforms are used to filter the strain data producing an output signal-to-noise ratio (SNR) timeseries. Peaks in the SNR time-series which pass a threshold of 4.0 are stored as “triggers”. These form candidates which may be coincident among two or more detectors or observed in only a single detector. Significance is assigned to each candidate using the likelihood ratio ranking statistic which is then mapped to a false alarm probability and corresponding FAR (Cannon et al. 2015). Candidates are finally uploaded to GraceDB after aggregating them across SVD bins by maximum SNR. GstLAL carries out both an early warning search, and a full bandwidth search. The early warning search targets low redshift BNS events that can be detected $\sim 10 - 60$ s before merger, using templates with non-spinning component masses between

⁶ For example, those hosted by SCiMMA and NASA

⁷ <https://emfollow.docs.ligo.org/userguide/>

0.95 M_\odot and 2.4 M_\odot (Sachdev et al. 2020). The full bandwidth search covers the entire CBC template bank parameter space.

GstLAL uses the multi-component FGMC method for assigning a probability of astrophysical origin to candidates (Kapadia et al. 2020; Farr et al. 2015). The probability that the signal originates from each CBC source category is also assigned. Triggers from each category (BNS, NSBH, BBH and terrestrial) are treated as realizations of independent Poisson processes. The rate of detectable triggers characterizing the Poisson process corresponding to each foreground category is approximated from the astrophysical rate estimates yielded by offline FGMC analyses of past observing runs while accounting for the change in sensitive spacetime volume between the past and ongoing runs. Misclassification among astrophysical source categories is accounted for by computing the probability of migration between injected and recovered templates across the entire bank semi-analytically under the Gaussian noise approximation (Fong 2018). With the rates and migration probabilities precomputed, p_{astro} is estimated in low-latency from trigger data comprising the likelihood ratio ranking statistic assigned to said trigger and the matched template.

2.1.2. MBTA

The Multi-Band Template Analysis (MBTA) pipeline carries out an early warning and main, full bandwidth search and performs matched filtering per frequency band to reduce computational costs (Aubin et al. 2021). The main instance of the pipeline is searching for binaries with total masses ranging from 2 to 500 M_\odot and mass ratio smaller than 50.

The pipeline includes signal-consistency checks to help distinguish astrophysical signals from background. As for the O3 offline analysis (Andres et al. 2022) the probability of astrophysical origin of GW candidate events is derived from the expected rate of astrophysical events and background candidates at the recovered chirp mass, mass ratio and ranking statistic. The foreground distribution has been estimated by performing injections of simulated BNS, BBH and NSBH signals into LIGO-Virgo O3a data which are then analyzed by the MBTA pipeline. This method computes p_{astro} and source classification. It has been extended to also provide EM-Bright information to determine the likelihood of an electromagnetic counterpart, as covered in Section 2.3.

2.1.3. PyCBC Live

PyCBC Live is a matched filtering pipeline designed to detect CBC events by comparing the incoming GW signal to a template bank of waveforms (Nitz et al. 2018;

Dal Canton et al. 2021). Two PyCBC Live searches were employed; one is a full bandwidth search for a wide range of signals, the other is an early-warning configuration for which the templates are truncated at certain frequencies before merger (Nitz et al. 2020). The full bandwidth template bank contains 412,575 templates, covering total masses from 2 to 500 M_\odot , and mass ratios from 1 to 100 (Roy et al. 2017, 2019). The early-warning template bank contains ~ 4700 templates with component masses in the range 1 to 3 M_\odot , truncated at a set of frequencies designed to give early warnings at regular intervals before the merger.

The matched filtering algorithm produces a time series of SNR values, and only triggers with $\text{SNR} \geq 4.5$ are considered for further analysis. The SNR is then re-weighted according to signal-consistency tests in each detector, and using multi-detector properties determined by the distribution of source extrinsic parameters (time difference, phase difference and amplitude ratios) for the signal population (Nitz et al. 2017).

In order to assess the frequency of a coincident noise signal which would be ranked greater or equal to a given detection, PyCBC Live assigns a FAR value by comparing the candidate to time-shifted background from the last several hours (Nitz et al. 2018). The FAR values for injections recovered during the MDC are subject to a substantial upward bias due to the high rate of high-SNR injected events, which significantly influences the background estimation.

For single-detector candidates, if strict criteria on signal consistency tests are passed, a FAR is assigned by comparing the candidate's re-weighted SNR to the noise trigger distribution via a template-dependent exponential fit (Dal Canton et al. 2021). The exponential fit is performed using the original data without injections, thus the FAR calculation for single-detector events is not subject to contamination from injections. Single-detector candidate signals are only considered for potentially electromagnetically bright signals, as BBH signals in low-latency are unlikely to yield multimessenger counterparts, and higher-mass templates are more susceptible to glitch contamination due to their shorter duration. Single-detector early-warning candidate signals are also not considered, as the poor localization of single-detector events is not of interest for pre-merger alerts.

For full bandwidth events, PyCBC Live also calculates the probability of astrophysical origin p_{astro} , based on the FAR value, the trigger SNR, the approximate distributions of signal and noise events over template chirp mass, and the sensitivities of observing detectors (Dent 2023). This p_{astro} is then combined with estimates of

the relative probabilities of different source classes, also based on template chirp mass; for details see [Villa-Ortega et al. \(2022\)](#).

In the later part of O3, an additional step was performed to optimize event SNR over template masses and spins ([Dal Canton et al. 2021](#)). Our MDC results include additional events produced via this optimization; however, it was removed from the search configuration deployed at the start of O4 in order to reduce complexity and computational load. We do not expect major differences in the search outputs detailed here due to the change.

2.1.4. SPIIR

The Summed Parallel Infinite Impulse Response (SPIIR) pipeline is designed to achieve lower delays in signal detection and differs from other pipelines in multiple aspects. As the name suggests, SPIIR uses a time domain counterpart of matched filtering ([Hooper et al. 2012; Luan et al. 2012](#)) as its primary filter. This method breaks down millions of CBC templates into a few hundred thousand IIR filters to perform match filtering in the time domain, further accelerated by the use of GPUs. The SPIIR pipeline implements a computational coherent network search approach ([Bose et al. 2000; Harry & Fairhurst 2011](#)) to select the GW candidate events with low-latency, achieved with the help of SVD ([Wen 2008](#)). The pipeline performs a full bandwidth search for BBH, BNS, and NSBH sources, and an early warning search for BNS and NSBH sources. SPIIR has demonstrated its performance in past LIGO-Virgo runs ([Chu et al. 2021; Kovalam et al. 2022](#)).

SPIIR is introducing a new two-step p_{astro} calculation for O4. In the first step, the pipeline calculates the two-component p_{astro} of the trigger based on the FGMC two-component method by [Farr et al. \(2015\)](#) and [Kapadia et al. \(2020\)](#). This assigns the probability of the trigger’s astrophysical or terrestrial origin. In the second step, it further classifies the probability of astrophysical origin into NSBH, BBH, and BNS, based on the chirp mass method ([Villa-Ortega et al. 2022](#)).

2.1.5. Coherent WaveBurst

Coherent WaveBurst (cWB) ([Klimenko et al. 2008, 2016; Drago et al. 2021](#)) is an excess power algorithm using minimal assumptions on the GW signature. cWB decomposes the GW strain data using a wavelet transform ([Necula et al. \(2012\)](#)). It then selects coherent signal power in multiple detectors and applies a maximum likelihood approach to select GW events. The calculation of the likelihood over the sky allows for building a sky map that characterizes the probability of the GW source sky location. A new feature with respect to O3

cWB analyses has been implemented for the significance assessment - a machine learning algorithm based on XGBoost ([Mishra et al. 2022; Szczepańczyk et al. 2023](#)). In low-latency, cWB analyzes 180 s data segments overlapping every 30 s. The alerts are created up to a latency of around 1 minute.

2.1.6. oLIB

The omicron-LALInferenceBurst (oLIB) pipeline is a short duration ($\lesssim 1$ second) unmodeled detection pipeline that is sensitive to a wide variety of sources that includes, but is not limited to, CBCs ([Lynch et al. 2017](#)). As such, oLIB makes very minimal assumptions about the astrophysical source type of the emission. The search is performed hierarchically. First, data from individual interferometers is analyzed with the Omicron trigger generator algorithm ([Robinet et al. 2020](#)). Omicron identifies regions in the time-frequency plane of excess power. Triggers that are coincident in time and frequency between interferometers are then followed up with a coherent Bayesian analysis using LIB. LIB models the data with a single sine-Gaussian wavelet, calculating two Bayes factors. Each of these Bayes factors is expressed as the natural logarithm of the evidence ratio of two hypotheses: (1) a GW signal versus Gaussian noise (BSN) and (2) a coherent GW signal versus incoherent noise transients (BCI). Ultimately, these two Bayes factors are used to construct a likelihood ratio Λ that is used as the final search statistic.

2.1.7. RAVEN

Rapid, on-source VOEvent Coincident Monitor (RAVEN) is a multi-messenger pipeline that searches for coincidence between GW candidates and other astronomical detections, such as gamma-ray bursts (GRBs) and neutrino bursts ([Urban 2016; Cho 2019; Piotrkowski 2022](#)). RAVEN ingests events submitted to the General Coordinates Network (GCN)⁸ ([Singer & Racusin 2023](#)) into GraceDB, queries GraceDB to look for a corresponding GW candidate, and calculates the joint false alarm rate to determine whether to send a public alert.

2.2. Selection of the public GW event candidate

When a potential GW signal appears in the detector, the low-latency search pipelines analyze the signal and produce event candidates. Each pipeline can report multiple candidates for a single GW signal. The event candidates, reported within a specific time window (1s around coalescence time for CBC searches,

⁸ <https://gcn.nasa.gov/>

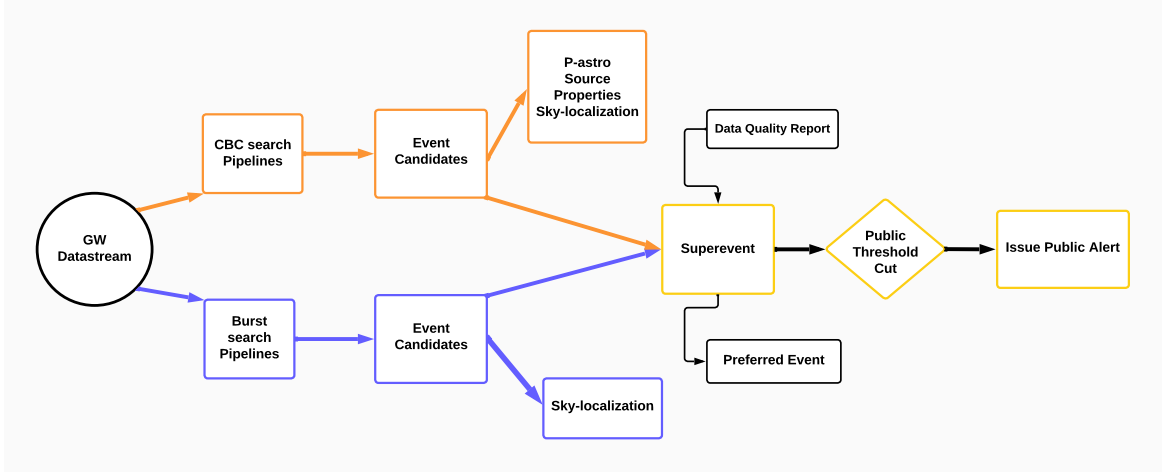


Figure 1. Task flow of low-latency alert infrastructure. The process begins with search pipeline trigger(s) on a candidate in the GW datastream, which are passed through data quality checks and compiled into a superevent. If the preferred event from the superevent passed the significant FAR cut, a preliminary alert is sent out to the public.

and 1 s around trigger time for burst searches), are collected and grouped as a *superevent*. In the collection, one GW event candidate is identified as the preferred event (defined as the event with the highest network SNR for CBC pipelines whereas lowest FAR for burst pipelines), and its properties and by-products are prepared for release to the public, which include the merger time, FAR, sky localization, and classification (see Section 2.3). Preferred event information may then be made public via an alert. Alerts are released publicly when a FAR passes the public alert threshold, currently $\text{FAR} \leq 2.31 \times 10^{-5} \text{ Hz}$ (two per day). An alert is labeled as *significant* when a CBC alert passes a FAR threshold of $\text{FAR} \leq 3.9 \times 10^{-7} \text{ Hz}$ (one per month) or when an unmodeled burst passes a FAR threshold of $\text{FAR} \leq 3.2 \times 10^{-8} \text{ Hz}$ (one per year). For CBC searches in the MDC, after including the trials factor that assumes six independent searches, this implies a threshold of $\text{FAR} \leq 6.4 \times 10^{-8} \text{ Hz}$ (one per 6 months) on individual candidates for publishing significant alerts⁹. Alerts that meet the public alert threshold but not the significant threshold are labeled *low significance*. RAVEN only uses the significant FAR thresholds when assessing its joint FAR for publication, with additional trials factors to compensate for listening to multiple GW pipelines.

2.3. Alert Contents

Public alerts are sent in order to inform the greater astronomical community of GW events to enable multi-messenger follow-up of these events. These alerts

are distributed via GCN and the Scalable Cyberinfrastructure to support Multi-Messenger Astrophysics¹⁰ (SCiMMA) project. The alerts come in two types: notices, which are machine-readable and come in a variety of formats, and GCN circulars, which are human-readable.

There are five types of notices that may be sent out for a candidate event: Early Warning, Preliminary, Initial, Update, and Retraction. Early Warning Notices arise from dedicated pre-merger search pipelines, potentially enabling the release of alerts seconds before merger (Magee et al. 2021). A first Preliminary Notice is sent out when an event candidate of a superevent exceeds the public FAR threshold. Following a timeout, the preferred event is determined and a second Preliminary Notice is then issued (even if the preferred event candidate remains unchanged). Both Early Warning and Preliminary Notices are sent out if the candidate passes automatic data quality checks; in certain cases, such as when manual data quality checks yield suspicions on the astrophysical nature of the candidate, a Retraction Notice may be sent. If, however, the Early Warning or Preliminary Notice passes human vetting, then an Initial Notice is sent out accompanied by a GCN Circular to announce the detection. The final type of notice, an Update Notice, is used to send out improved estimates of alert contents based on parameter estimation if they become available. Included in each alert is an estimate of the event’s probability of astrophysical origin, or p_{astro} . This is broken up into four categories that sum to 1 by definition: $P(\text{BNS})$, $P(\text{NSBH})$, $P(\text{BBH})$, and

⁹ At the time of writing, there are five independent CBC searches used in the observing run for a threshold of $\text{FAR} \leq 7.7 \times 10^{-8} \text{ Hz}$ (one per 5 months).

¹⁰ <https://scimma.org/>

P(Terrestrial), where the mass boundary between NS and black hole (BH) is set at $3 M_{\odot}$. If the superevent is coincident with a GCN candidate, the various data products concerning the joint candidate are included, such as the time delay, joint FAR, and combined sky map if applicable.

Sky localization—One of the key data products to enable multi-messenger follow-up is the rapid inference of the sky localization from GW observations. This sky localization consists of the posterior probability distribution of the source location in the sky. The sky localization, mapped either over a 2D map of right ascension and declination, or a 3D volume which also includes a distance estimate, is known as a “sky map.” Sky localization (and parameter estimation more generally) is conducted in multiple stages once a candidate is identified.

For CBC sources, BAYESian TriAngulation and Rapid localization (BAYESTAR), a rapid sky localization algorithm (Singer & Price 2016), is used to generate sky maps, and may be updated by Bilby (Section 2.4), a python-based parameter estimation pipeline that uses stochastic sampling methods (Ashton et al. 2019; Romero-Shaw et al. 2020). Sky maps from BAYESTAR are released with Preliminary Notices and sky maps from Bilby are released in Update Notices. Additionally, cWB also generates localizations (Klimenko et al. 2011).

The sky map is stored as FITS file using the Hierarchical Equal Area isoLatitude Pixelization (HEALPix) (Górski et al. 2005) framework in the Multi-Order Coverage (MOC) representation (Fernique et al. 2014); flattened versions at a fixed HEALPix grid size are also available for superevents. MOC sky maps use adaptive division of the HEALPix grid, focusing areas of highest resolution on regions of highest probability with minimal information loss. Sky maps are made available both through the distributed alert as well as uploaded on GraceDB, where they are available for direct download. If there is a coincidence with a GRB candidate that has a sky localization, we use this to re-weight the GW sky map and include this combined sky map in the alert as well.

EM-Bright—EM-bright is a pipeline designed to assess whether a GW candidate is capable of producing an electromagnetic counterpart. A rapid assessment of EM-bright properties, **HasNS** and **HasRemnant**, is essential to trigger target of opportunity (ToO) follow-up by ground and space-based observatories. In this regard, **HasNS** and **HasRemnant** quantities are reported as a part of the automated and update discovery notices.

The **HasNS** is the probability of the binary having a NS component, while **HasRemnant** is the probability of the merger leaving remnant matter post-merger in the form of dynamical or tidal ejecta.

The exact nature of EM emission from the merger is complex and depends on several factors like the properties of the ejecta, the NS EoS, and the BH mass and spin. Detailed analyses are required to assess the accurate properties of EM counterparts (see, for example, Shibata & Hotokezaka (2019) for a review). These are, however, impractical in a real-time setting. Aside from theoretical uncertainties, measurement uncertainties predominantly affect the assessment of EM-brightness in real-time. Note that the only real-time data product available from match filter CBC searches is the template parameters that maximize the likelihood of detection. Bayesian parameter estimation from computationally cheap waveform models may be available in \sim hours, as discussed later, but it is not available in the seconds after a trigger is registered. Hence, inference from the template parameters and real-time detection statistics is the feasible solution.

To this end, Chatterjee et al. (2020) showed the application of supervised machine-learning trained on a feature space involving the template parameters and detection statistics to make this inference. Training is done using large-scale simulation campaigns where the ground truth and the recovery of search pipelines are registered. The ground truth is labeled based on its intrinsic source-frame mass as having a NS component, or both mass and spin components as leaving remnant matter behind post merger, based on a phenomenological fit to numerical relativity simulations by Foucart et al. (2018). The NS EoS plays a crucial role in the labeling as stiffer EoS favor tidal disruption, and therefore prefer larger ejecta masses. While in Chatterjee et al. (2020) a single, stiff NS EoS was used on conservative grounds, here we extend the analysis to multiple EoSs, and reweight the score based on Bayes factors computed against GW170817 (LVK 2018) tidal deformability measurements for several literature NS EoSs presented in Ghosh et al. (2021). The score presented is therefore marginalized over several EoSs.

In addition to **HasNS** and **HasRemnant**, a new quantity **HasMassGap**, the probability that at least one component of the binary merger is in the lower mass-gap region i.e. source-frame mass between $3 M_{\odot}$ to $5 M_{\odot}$ is computed. The technique used in computing **HasMassGap** is similar to the original EM-bright quantities, except the labeling is different and does not involve the knowledge of the NS EoS. The values reported for **HasNS** and **HasRemnant** use a nearest-neighbor classifier algo-

GstLAL Chunks used for Training HasMassGap Classifier

Start date	End date
Sun 2017-01-22 08:00:00 UTC	Fri 2017-02-03 16:20:00 UTC
Tue 2017-02-28 16:30:00 UTC	Fri 2017-03-10 13:35:00 UTC
Fri 2017-06-30 02:30:00 UTC	Sat 2017-07-15 00:00:00 UTC
Sat 2017-08-05 03:00:00 UTC	Sun 2017-08-13 02:00:00 UTC
Sun 2017-08-13 02:00:00 UTC	Mon 2017-08-21 01:05:00 UTC

Table 1. Calendar times for the detector chunks of LIGO O2 data. We consider the mass-gap injections performed by the GstLAL search in these duration along with previously existing set in Chatterjee et al. (2020) for the study.

rithm, while that used for HasMassGap use a random-forest classifier algorithm. The dataset used for training contains additional mass-gap injections done separately on O2 dataset whereas the feature space used to train the algorithm is the same as Chatterjee et al. (2020) – a five-dimensional space involving the triggered template masses $m_{1,2}$, the aligned dimensionless spins, $\chi_{1,2}$, and the network SNR. The duration from which the mass-gap injections were taken from is shown in Table 1.

Similar to the sky maps, these quantities are *updated* from online parameter estimation samples, which are available \sim hours after discovery. The parameter estimation samples allow for these quantities to be computed directly.

2.4. Low-latency Parameter Estimation

CBC signal candidates labeled as significant (see 2.2) are further investigated via automated Bayesian parameter estimation analysis with the Bilby library. It employs the nested sampling technique implemented in the Dynesty library (Speagle 2020) to explore the full parameter space of masses and spins, producing accurate inference results immune to biases included in the point estimates of masses and spins from search pipelines. It also takes into account uncertainties in detector calibration and marginalizes the posterior probability distribution over them.

To accelerate the analysis, we employ the reduced order quadrature (ROQ) technique (Canizares et al. 2015; Smith et al. 2016; Morisaki & Raymond 2020), which approximates gravitational waveform with ROQ basis elements to reduce the computational cost of likelihood evaluations. The ROQ basis elements employed in the automated parameter estimation of O4 are presented in Morisaki et al. (2023).

For BNS candidates, the analysis assumes that dimensionless spins have norms less than 0.05 and are aligned

with the orbital angular momentum, and employs the IMRPhenomD waveform approximant (Husa et al. 2016; Khan et al. 2016) to recover the observed signals. This analysis typically takes less than ten minutes and enables updating sky localization within an hour including the initial timeout to start parameter estimation and time spent for post processing. In addition to this automated analysis, more costly manual analyses incorporating general spin configurations and tidal deformation of colliding objects may follow, depending on the significance of the signal. For candidates with higher masses, the automated analysis takes into account general spin configurations, and employs IMRPhenomXPHM (Pratten et al. 2021) if its ROQ basis elements are available in the target mass range, and IMRPhenomPv2 (Hannam et al. 2014) otherwise. This analysis typically takes hours to complete. The output of this analysis is released as an Update Notice.

3. MOCK DATA CHALLENGE

To create a background for the MDC, we consider the stretch of data taken between Jan 05, 2020 – Fri Feb 14, 2020 by the LVK instruments during O3. A total of 5×10^4 simulated CBC waveforms with mass and spin distributions mentioned in Table 2 are injected into the O3 data with an interval of ~ 1 minute between injections. The optimal network SNR is greater than 4 for all the injections. This is done to prevent “hopeless” injections, which are improbable to be detected in reality. The IMRPhenomPv2_NRTidalv2 waveform approximant is used to consider matter effects in case of NS components of the injections. For BHs, the same waveform is used with the tidal parameters set to zero. In order to label a component as a NS, the SLy (Chabanat et al. 1998) NS EoS is used, which allows for a maximum mass of $\sim 2.05 M_\odot$. Hence, in this scheme, the tidal deformability of component masses above this limit are set to zero consistent with being a BH. In particular, all injections above the SLy maximum mass are assumed to be BHs, and the appropriate relative rate is used for the same. These injected signals are primarily recovered by CBC pipelines, and occasionally by Burst pipelines. In the MDC exercise, we have focused most of our analysis on the output and data products of the CBC pipelines. We also note that the injection rate density used in the study is artificially high and not representative of the true discovery rate in O4. Therefore, quantities like p_{astro} which rely on the background distribution, may not be the true representation as compared to a real-

Compact Object Properties					
Binary Type	Object	m/M_\odot (min/max)	m distribution	Max a	a distribution
BNS	Primary	1.0 - 2.05	uniform	0.4	uniform & isotropic
	Secondary	1.0 - 2.05	uniform	0.4	uniform & isotropic
NSBH	Primary	1.0 - 60.0	m^{-1}	0.998	uniform & isotropic
	Secondary	1.0 - 2.05	uniform	0.4	uniform & isotropic
BBH	Primary	2.05 - 100	$m^{-2.35}$	0.998	uniform & isotropic
	Secondary	2.05 - 100	m^1	0.998	uniform & isotropic

Table 2. Distribution of intrinsic properties (component masses m and spins a) of binary systems in the injection sample. The spin distributions are uniform in magnitude and isotropic in orientation, as seen in the last column.

istic signal density. The CBC injection set consists of 40.9% BNS, 35.8% NSBH, and 23.3% BBH injections.

The events are distributed uniformly in co-moving volume assuming flat Λ CDM cosmology with $H_0 = 67.3 \text{ km s}^{-1} \text{ Mpc}^{-1}$ and $\Omega_m = 0.3$ based on Planck 2018 results mentioned in Table 1 of [Aghanim et al. \(2020\)](#). The BNS systems are distributed up to a maximum redshift of $z = 0.15$, the neutron-star black-hole systems up to $z = 0.25$, and the BBHs up to $z = 1.9$. The simulated strain is projected on to the detector geometries, shifted in time to the time of experiment and streamed as 1 s segments for the search and annotation pipelines to analyze in real-time (see Section 2.1). The triggers and their annotations were reported in *GraceDB* for post processing studies.

This exercise is repeated in several cycles for benchmarking analysis and will continue internally during the observing run to continuously track improvements in the alert infrastructure and provide avenues for pipelines to test their changes. The numbers reported here are those from a single cycle of 5×10^4 injections where the status of most analyses were close to their O4 configurations.

4. RESULTS

4.1. Pipeline Performance

In order to demonstrate LLAI readiness for O4, we compare CBC triggers and their corresponding data products uploaded to *GraceDB* with the injection set. Triggers and injections are matched using the merger time; all triggers within 1 s of an injection are matched to that injection and included in the analysis. This process removes noise triggers between injections and ensures trigger times correspond to an injection time window. It is possible for a few noise triggers to be coincident with injection time window. Matching triggers to injections allows us to evaluate data products by comparing the results with the injected quantities. These data products include basic parameter estimates, sky maps, and p_{astro} values. However, not all injections are recovered

in the form of trigger. There are four main reasons why an injection may not be found by the search pipelines: (i) some injections are distant or have a low SNR, due to the cosmological distribution preferring larger distances, and can not be distinguished from background noise, (ii) there are stretches of the O3 replay where one or more detectors were not operational and in science mode, (iii) there were some temporary technical issues on computing resources used during this MDC cycle, and (iv) there may be data quality issues that overlap with an injection, such as loud or long glitches.

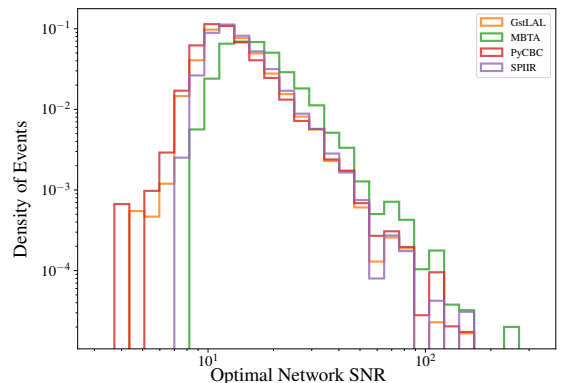


Figure 2. Histograms of the optimal, or injected, network SNR, normalized for each CBC pipeline, for triggers below the significant FAR threshold. All pipelines were found to recover injections across the range of injected SNR values.

As mentioned in the previous section, for this analysis we focus on the MDC cycle used for the review of pipeline performance, which ran from February 16 through March 28, 2023 consisting of 5×10^4 injections. During this MDC, 1489 BNS, 1105 NSBH, and 1920 BBH injections were recovered. As seen in Figure 2, each of the CBC search pipelines, PyCBC, GstLAL, MBTA, and SPIIR, successfully uploaded events below the significant FAR threshold across the range of injected SNR values. Burst searches, cWB and oLIB, make little as-

assumptions of source type, and so are only considered for measures of latency in this paper. We plot the simulated vs. recovered network SNR in Figure 3. In general, signals with moderate to high SNR are recovered well, with some bias at low SNRs due to the FAR threshold imposed for upload. Additional scatter in SNR recovery is expected since the simulated optimal SNRs were calculated using fixed detector sensitivities, whereas actual detector data has significant fluctuations in sensitivity over time. The optimal SNRs for injections are calculated using a global average PSD, instead of using a local estimate of the PSD, which may cause some of the off-diagonal outliers.

For the 4514 GW injections found, we created 469 multimessenger coincidences by injecting simulated GRB candidates at times surrounding the GW injections. We found 356 of these joint candidates triggered a RAVEN alert as a result of passing the *significant* FAR threshold.

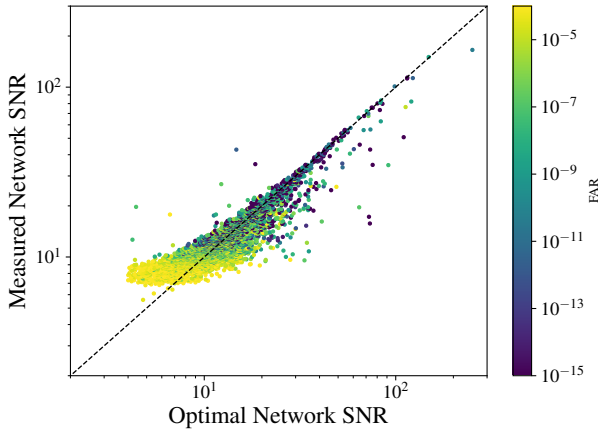


Figure 3. The measured network SNR recovered during the MDC compared to the optimal, or injected, network SNR with the points colored by FAR. We find SNR is recovered more accurately for higher values.

4.2. Latency Measures

Due to the desire for timely follow-up by the multimessenger community, a key feature of the LLAI is dissemination of results as quickly as possible. The goal for the LLAI system is to send alerts for events within 30 s of merger time; this number sets the timescale for comparison below. Here, we perform a systematic study of the alert latency for three of the key pieces of the pipeline (a fourth, the data calibration, construction, and transfer between sites, which takes ~ 10 s, is not captured here, as well as latency from the ingestion and redistribution by GCN or SCiMMA). Latency comes primarily from these three components: (i) the search

Latency Measure	Description	50% (s)	90% (s)
Superevents	$t_{\text{superevent}} - t_0$	9.4	18.1
CBC Events	$t_{\text{event}} - t_0$	12.3	41.4
Burst Events	$t_{\text{event}} - t_0$	72.3	671.3
Early Warning Events	$t_{\text{event}} - t_0$	-3.1	2.9
GW Advocate Request	$t_{\text{ADV_REQ}} - t_0$	12.7	40.1
GCN Preliminary Sent	$t_{\text{GCN_PRELIM}} - t_0$	29.5	171.4
Coincidence with GRB Found	$t_{\text{EM_COINC}} - t_0$	32.9	44.4
RAVEN Alert Triggered	$t_{\text{RAVEN_ALERT}} - t_0$	35.3	48.4

Table 3. Measured latencies for a number of steps in the pipeline. t_0 corresponds to the event merger time reported by the pipeline, while $t_{\text{superevent}}$ and t_{event} correspond to the time of superevent or event creation. For the case of superevent latencies, t_0 is determined by the preferred event.

pipelines, (ii) the event orchestrator `gwcelery`, and (iii) `GraceDB`. We note that technical issues during the MDC may also cause some high-latency outliers, so the results presented are conservative when excluding the time needed for transfer and construction of the strain data.

To calculate event latencies, we compare the time an event is created and appears on `GraceDB` to that of the known merger time. For CBC pipelines, we find a median (90%) latency of 12.3 s (41.4 s); for Burst pipelines, we find a median (90%) latency of 72.3 s (671.3 s). We then compare this number to the creation of a superevent; we find a median (90%) latency of 9.4 s (18.1 s). The median superevent latency is lower than the event latency simply due to the fact that the superevent may be created upon the first trigger, and that a superevent often consists of multiple events. We also make the same measurement for Early Warning alerts, shown on the right of Figure 4; we find a median (90%) latency of -3.1 s (2.9 s). Considering the joint candidates, we find that it takes a median (90%) latency of 32.9 s (44.4 s) to find a coincidence with a GRB injection and a median (90%) latency of 35.3 s (48.4 s) to trigger a RAVEN alert.

Once the event(s) have been created, there is a request for human vetting of the alert, called the Advocate Request; we find a median (90%) latency of 12.7 s (40.1 s) to notify the advocate. To measure the latency of event communication to the community, we also measure the latency for sending of the GCN preliminary alert, which occurs for superevents that pass automated data quality checks; we find a median (90%) latency of 29.5 s (171.4 s). This latency reported specifically measures that time until the GCN preliminary label is applied. We show this statistic for GCN preliminary alerts on

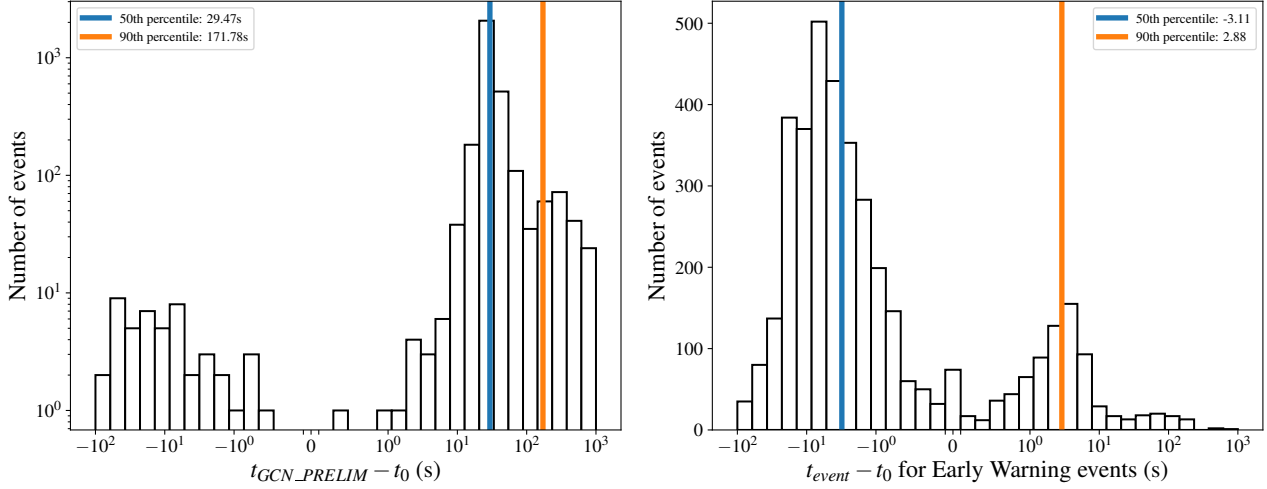


Figure 4. *Left:* Histogram of latencies for the sending of the GCN preliminary alert. *Right* Histogram of latencies for Early Warning alerts. t_{GCN_PRELIM} corresponds to the time the GCN preliminary alert is sent, t_0 corresponds to the preferred event merger time, and t_{event} corresponds to the time of event creation.

the left of Figure 4. Table 3 shows a compilation of these latency statistics for comparison. The number of candidate events within a superevent was not shown to have a noticeable effect on the latency of that event and its corresponding preliminary alert.

4.3. Probability of astrophysical origin

Each CBC pipeline uploads its own estimate of p_{astro} , as described in Section 2.1, and is inherited by the superevent if the event is the preferred event. By matching the MDC’s injected parameters to the recovered p_{astro} values from pipelines, we can test the accuracy of p_{astro} . Figure 5 shows the recovered $P(\text{source})$ for true sources (e.g., $P(\text{BNS})$ for true injected BNS events), for superevents which pass the public alert FAR threshold. In matching these injections, we place the cut between NS and BH at $3 M_{\odot}$. “True” terrestrial events correspond to superevents which were not temporally matched to injections, indicating that they arose from detector noise. Injected BBHs are typically recovered confidently, with the vast majority resulting in $P(\text{BBH}) > 0.5$. Over 90% of BBHs are recovered with $P(\text{BBH}) > 0.9$. The $P(\text{BNS})$ and $P(\text{NSBH})$ distributions are less confident than the $P(\text{BBH})$ distribution; about 10% of true BNSs and NSBHs are recovered with $P(\text{BNS})$ or $P(\text{NSBH}) < 0.1$. As a check against contamination across $P(\text{BNS})$ and $P(\text{NSBH})$ due to errors in recovered masses or variation in the definitions of the mass border between NS and BH (i.e., the Tolman–Oppenheimer–Volkoff mass), we can also look at the distribution of the sum of $P(\text{BNS})$ and $P(\text{NSBH})$ for injected events where $m_2 \leq 3M_{\odot}$. This is shown in the bottom panel of Figure 5. Compared to $P(\text{BNS})$ or $P(\text{NSBH})$ alone, $P(\text{BNS}) + P(\text{NSBH})$ performs slightly better, with $\sim 75\%$ of true BNS or NSBHs

receiving $P(\text{BNS}) + P(\text{NSBH}) > 0.9$, compared to 60% and 65% for NSBH and BNS respectively. If instead we use a threshold $P(\text{source})$ of .5, we find a TPR of $\sim 98\%$ for BBH, $\sim 90\%$ for BNS, and $\sim 76\%$ for NSBH injections.

4.4. Sky localization

In order to evaluate localization performance, in the following, we focus on three metrics: (i) localization area, (ii) retrieved median distance of the source, and (iii) searched area. Localization area is the area (measured in deg^2) which encloses a given probability contour in the sky map; in this paper, we use 90% as the total cumulative probability threshold. Retrieved distance refers to the median of the distance distribution along the line of sight of the injected sky position. Searched area is the smallest 2D area, starting with the regions of highest probability, that contains the true location of the source; it represents a measurement of the sky area that a telescope with a small FOV relative to the sky map size would need to cover before imaging the true location. We refer the reader to [Singer & Price \(2016\)](#) for more details on these parameters, and use the `ligo.skymap`¹¹ package to compute all metrics.

When evaluating sky map performance, we consider the preferred events for superevents that fall under the significant FAR threshold before trials factor and were detected by more than one interferometer. We exclude single detector triggers as most resulted from injections that occurred during a portion of O3 replay data where one or more detectors was not in science mode, and they

¹¹ <https://git.ligo.org/leo-singer/ligo.skymap>

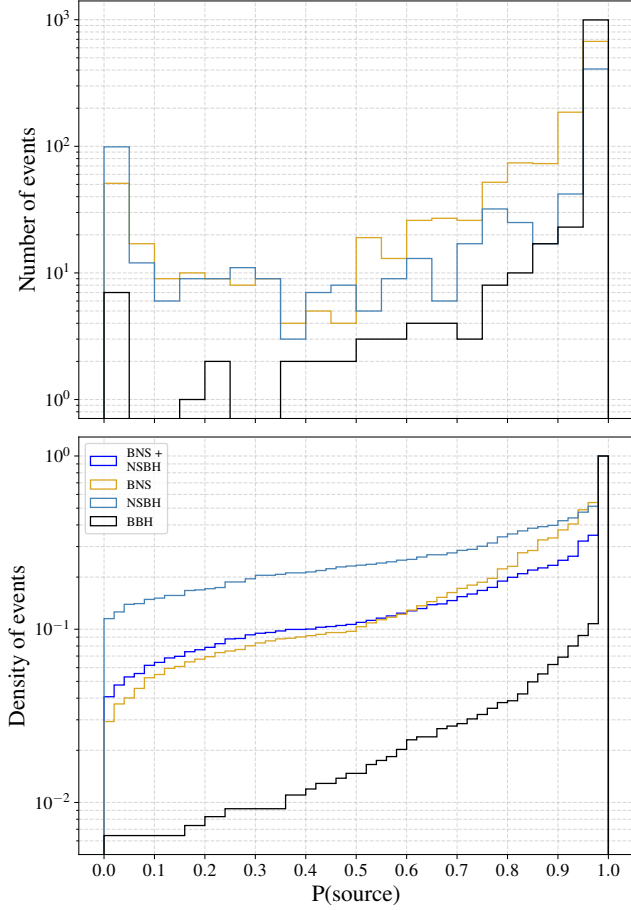


Figure 5. *Top:* Histogram of “preferred” recovered $P(\text{source})$ for true sources, for superevents which pass the significant public alert threshold. The possible source classes are BNS, NSBH, and BBH. This excludes early warning events, which were not fully functional during the time of this analysis. *Bottom:* Cumulative density of the same data. We also include the distribution of correctly recovered BNS or NSBH, which checks for contamination between the two classes due to misrecovered secondary masses or effects from varying the NS/BH mass boundary. As this is a cumulative histogram, the fraction of events above a certain $P(\text{source})$ corresponds to the TPR. We see that the majority of events with a $P(\text{source})$ greater than 0.5 correctly recover the injection source type.

may have sky localizations on the order of the entire sky. For Figure 7, We also exclude a slice of parameter space for injected NSs of mass $\leq 2M_{\odot}$ with spins $\geq .05$, as these events may not have a match within the pipeline template banks. We compare the 90% localization area with the recovered distance in Figure 6.

We see that typically for smaller retrieved distances of the injection, the localization areas too were small. The same trend was seen for the searched areas for these superevents, where at higher distances one would typically

encounter higher searched areas, which aligns with the expected behaviour. Further, in the top panel of Fig 7, we show the accuracy of BAYESTAR sky maps through a P - P plot. P - P plots of this format show the fraction of injections found within a given credible interval across all levels of credible intervals. The three gray lozenges around the diagonal shows the three different levels of confidence ($1-3\sigma$) for the combined BAYESTAR map sample. We find that the BAYESTAR sky maps fall just outside the credible intervals for higher credible intervals. This tells us BAYESTAR slightly overstates the precision of its sky localizations. We also show the performance of different pipelines that detected the preferred event in the given sample. See the appendix for a discussion of sky map performance for each individual pipeline. In the bottom panel of the Figure 7, we show the cumulative trend of the searched area statistics from the combined sample. We find a median searched area of $100 - 200 \text{ deg}^2$. We then compare the two interferometer events with the three interferometer events, to show that the latter produced smaller searched areas.

Further, we probed the accuracy of the BAYESTAR sky maps compared with Bilby sky maps for BNS events. This comparison P - P plot and searched area histogram can be seen in Figure 8 for the preferred event of all BNS superevents for which both sky maps were produced. In this figure, we include the events excluded in Figure 7 to demonstrate Bilby’s performance even without the cuts. A plot with those cuts applied can be found in the appendix. From the top panel of Figure 8, we see that the BAYESTAR sky maps tend to sag below Bilby’s implying that their precision was overstated as compared to Bilby. There is a trade-off between the latency of BAYESTAR sky maps available with the Preliminary GCN alert, and the improved accuracy of the Bilby sky maps that are available with the completion of parameter estimation. The cumulative searched area plot in the bottom panel of Figure 8 shows that typically Bilby sky maps have lower searched area by factor of 2 or more.

4.5. EM-Bright

We show the performance of the EM-Bright classifiers across all four CBC pipelines via their Receiver Operating Characteristic (ROC) curves. For this, the NSBH boundary is chosen according to SLy EoS but the probabilities are EoS marginalized, meaning we include some uncertainty in the NS EoS in our classifications. The markers indicates three different representative thresholds (a score above which events are considered to be positively classified as the source type in question) along the ROC curves for each pipeline. In

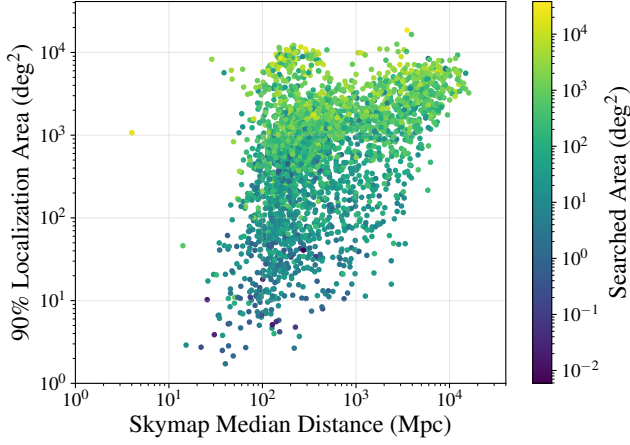


Figure 6. Sky localization distribution as a function of recovered median distance from the sky map, with the trend of Searched Area for the preferred event. We find the more distant the event, the larger is the localization area. The color bar shows that the searched area associated with the event also increases with the localization area and sky map median distance as discussed in Section 4.4.

Figure 9, we see that the `HasRemnant` quantity for all four pipelines has greater than a 95% TPR for a 5% False Positive Rate (FPR). In the middle panel, we see (`GstLAL`, `PyCBC`, `MBTA`) perform consistently at $\sim 97\%$ TPR at $\sim 3\%$ FPR for `HasNS` classifier. The `SPIIR` pipeline purity is slightly lower compared to the other pipelines, $\sim 90\%$ TPR at the same misclassification fraction. One possible mitigation technique is to use more training data from the pipeline in the training process. In the last panel, for `HasMassGap`, we see (`GstLAL`, `SPIIR`, `MBTA`) perform with $\sim 80\%$ TPR at $\sim 20\%$ FPR while `PyCBC` lags slightly below. We expect to enhance the performance of these classifiers further in the near future by retraining the classifiers using the O3 MDC data.

5. CONCLUSION

In this paper, we present the performance of the low-latency alert infrastructure and associated data products based on the O3 MDC. A large simulation campaign of compact binaries i.e. BNS, NSBH, and BBH are injected into a stretch of real data from O3. The data is taken through the entire end-to-end alert infrastructure starting from the search pipeline, data products computation, and alert generation. We demonstrate that for full bandwidth searches automated preliminary alerts, excluding time for data transfer and construction, are delivered with a median latency of $\lesssim 30$ s, which is an improvement since O3 (Abbott et al. 2021b). We show that low-mass BNS injections are successfully detected by early warning searches. Annotations and alert de-

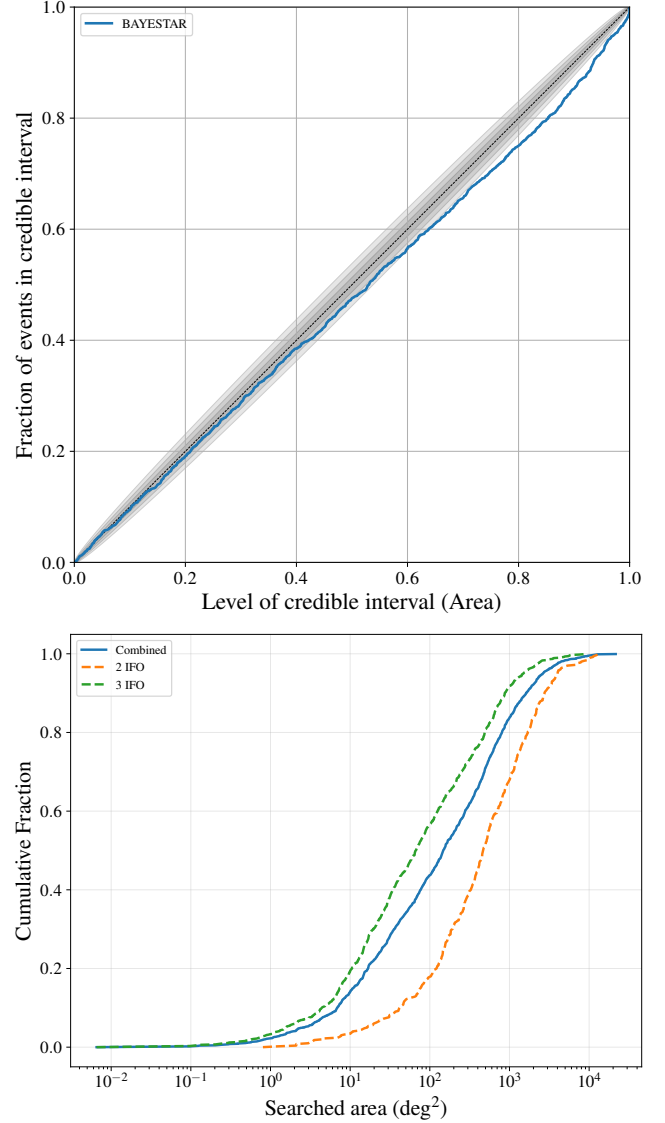


Figure 7. *Top:* A P - P plot showing the BAYESTAR sky map statistics for the preferred event. The credible intervals shown in gray are based on the total number of events. *Bottom:* Cumulative histograms of searched area for all events (blue), along with two subsets of two-interferometer (Orange) & three-interferometer (Green) events. We see that the three-interferometer events produced smaller searched areas than the two-interferometer events by almost an order of magnitude as discussed in Section 4.4.

livery is achieved for a significant fraction of such signals before merger time with a median alert latency of ~ -3 s. It is to be noted however, that alert delivery before merger time does not happen for all early warning events. In addition, through the use of this MDC dataset, we demonstrate that the data products, pro-

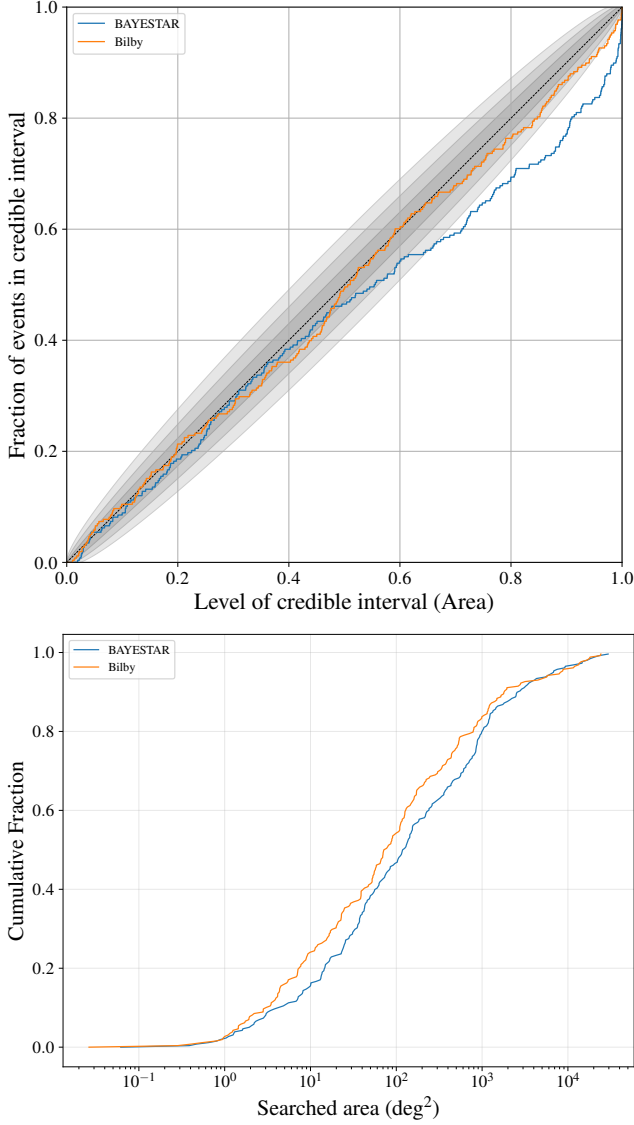


Figure 8. *Top:* A P - P plot showing the performance of BAYESTAR (blue) and Bilby (orange) generated sky maps for BNS events. The credible intervals shown in gray based on the total number of such preferred events where both BAYESTAR and Bilby sky maps are available. *Bottom:* Cumulative histograms showing searched area statistics for BAYESTAR and Bilby sky maps. We observe that Bilby sky maps give a lower searched area and tend to be more precise than their BAYESTAR counterparts as discussed in 4.4.

duced in the same workflow as planned for O4, are statistically consistent with simulated values.

The p_{astro} values giving probability of an astrophysical BBH, BNS, or NSBH were found to correctly classify the source for the majority of events. For a threshold $P(\text{source})$ of 0.5, we find a TPR of $\sim 98\%$ for BBH, $\sim 90\%$ for BNS, and $\sim 76\%$ for NSBH injections.

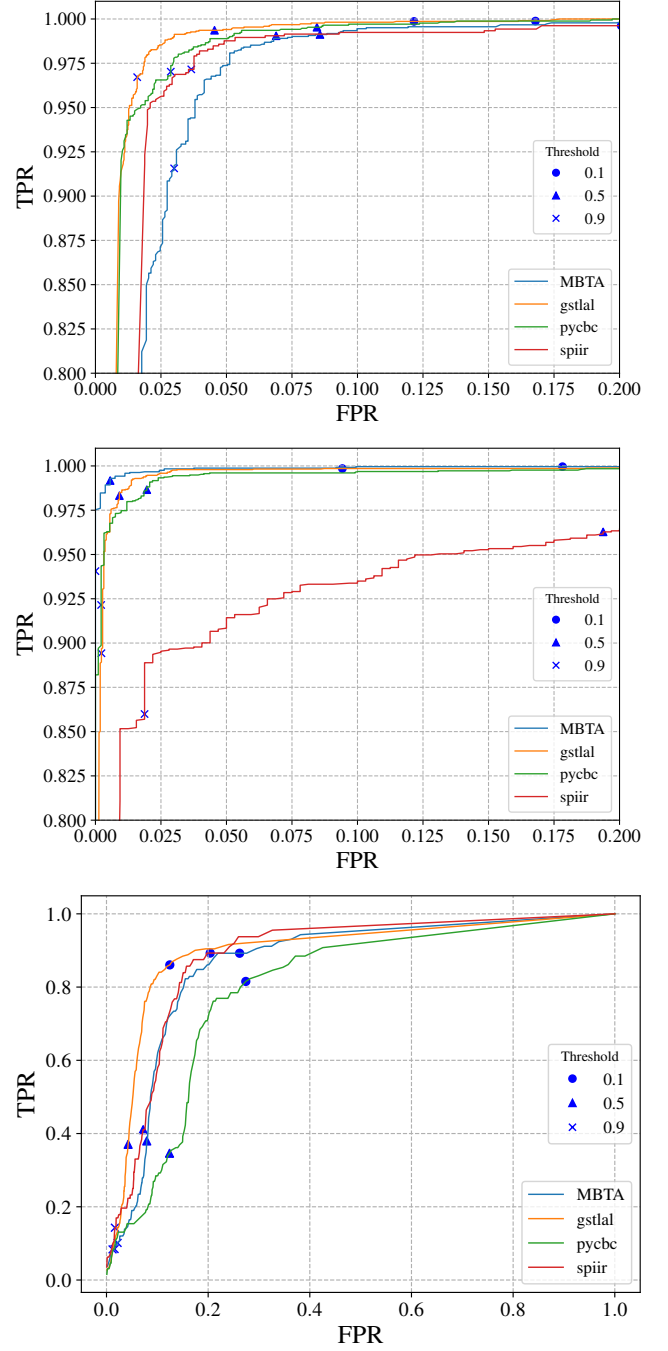


Figure 9. The ROC curves for the different EM-Bright classifiers are shown here for MDC 11 events. The top, middle, and bottom panels refer to HasRemnant, HasNS, and HasMassGap quantities respectively. The markers denote different representative thresholds along the curve.

The distribution of injected sky positions is found to be well recovered by the sky maps produced by both BAYESTAR and Bilby, as evidenced by Figs. 7 and 8. BAYESTAR provides low-latency sky maps that slightly overstate the precision, while Bilby provides improved

accuracy upon completion of parameter estimation. The median searched area is found to be $100\text{--}200\text{ deg}^2$, with slight variations between method and pipelines. We observed that **Bilby** sky maps have better precision, and typically gave a smaller searched area.

The EM-Bright values corresponding to the probabilities of **HasNS** and **HasRemnant** have a TPR of above $\sim 95\%$ at $\sim 5\%$ FPR across GstLAL, PyCBC, MBTA pipelines. The SPIIR pipeline is performing similarly for **HasRemnant** but its performance is slightly lower for **HasNS**. **HasMassGap**, on the other hand, has a TPR of above $\sim 80\%$ at $\sim 20\%$ FPR.

This paper presents the low-latency data products for O4 and their expected performance. Additional data products that expand on the current EM-Bright products for determining the likelihood of a kilonova are being developed that include predictions of mass ejecta for BNS and NSBH events, as well as peak magnitudes for corresponding kilonovae. We hope to make these data products public in the future.

We thank Varun Bhalerao for review of this paper. We thank the MBTA team for their contributions and for allowing the use of their pipeline data.

AT, AG, and MWC acknowledge support from the National Science Foundation with grant numbers PHY-2010970 and OAC-2117997. SSC and MC acknowledge support from the National Science Foundation with grant number PHY-2011334 and PHY-2308693. MC would also acknowledge support from NSF PHY-2219212. DC would like to acknowledge support from the NSF grants OAC-2117997 and PHY-1764464. EK, EM, GM would like to acknowledge support from NSF grant PHY-1764464. SM acknowledges support from JSPS Grant-in-Aid for Transformative Research Areas (A) No. 23H04891 and No. 23H04893. SA thanks the MITI CNRS for their financial support. SG acknowledges NSF PHY-2110576. NA, PB, AB, PB, YKC, CM, and JC acknowledges NSF PHY-2207728. TD and VVO have received financial support from Xunta de Galicia (CIGUS Network of research centers), by European Union ERDF and by the “María de Maeztu” Units of Excellence program CEX2020-001035-M and the Spanish Research State Agency, and are supported by the research grant PID2020-118635GB-I00 from the Spanish Ministerio de Ciencia e Innovación.

APPENDIX

A. SKY MAP PERFORMANCE

The additional plots shown in this section are provided to demonstrate **Bilby** and **BAYESTAR** produce accurate sky localizations from injections found by each individual CBC pipeline. Figure 10 shows the **BAYESTAR** performance of preferred events from each pipeline falls within the credible intervals besides minor deviations, and uses the same set of events and cuts as found in Figure 7 and discussed in Section 4.4. To demonstrate performance for the events most likely to be subject to extensive follow-up, Figure 11 specifically presents only BNS injections that pass the cuts applied in Figure 7. With these cuts we find the combined performance for both **Bilby** and **BAYESTAR** falls within for within credible intervals.

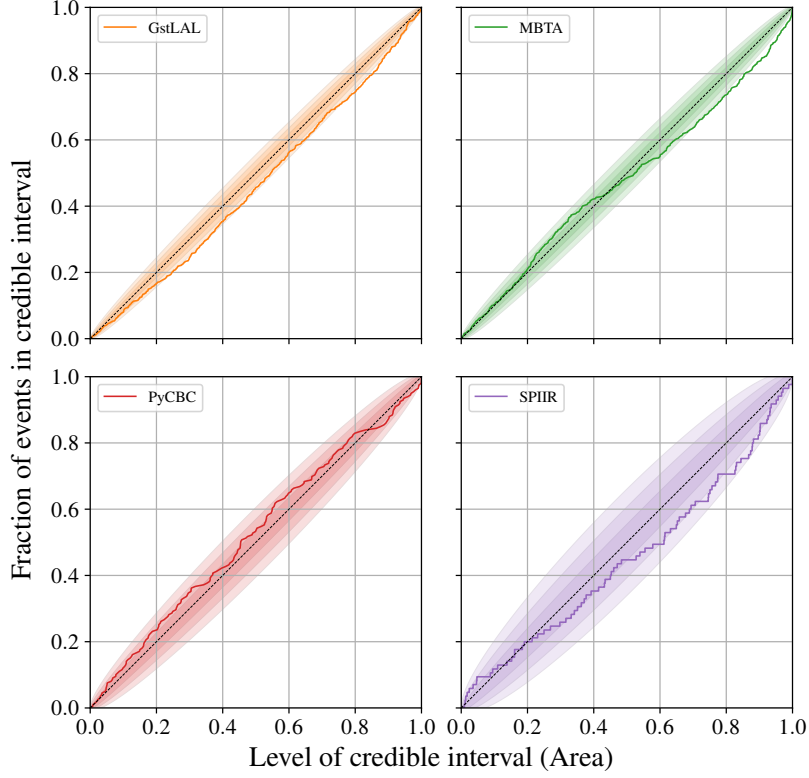


Figure 10. P - P plots showing **BAYESTAR** performance for pipelines that detected the preferred event. All the sky maps generated show that the performance of the sky maps are within the confidence bands.

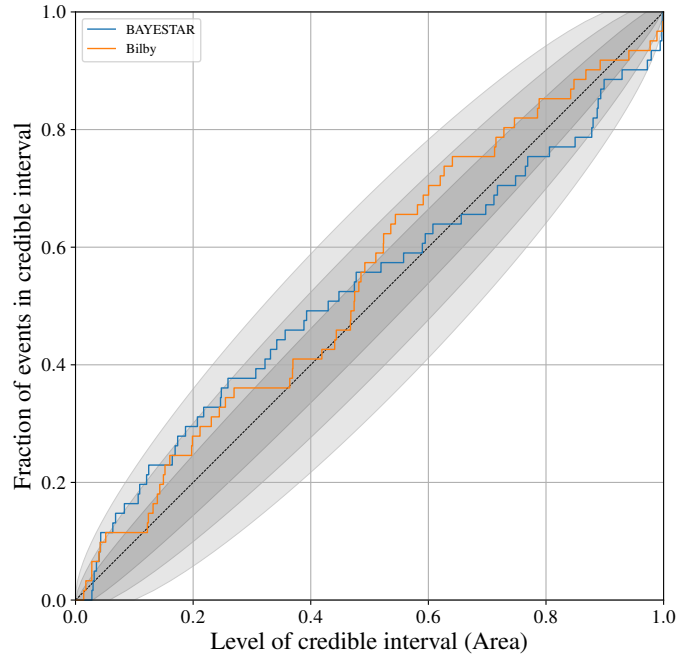


Figure 11. P - P plot comparing the performance of **Bilby** and **BAYESTAR** for BNS injections likely to be the subject of follow-up, including the cuts on mass, spin, FAR, and number of interferometers as covered in Section 4.4. We see both **Bilby**'s and **BAYESTAR**'s performance is improved and within the credible intervals when including these cuts.

REFERENCES

- Abbott, B. P., et al. 2017a, *Phys. Rev. Lett.*, 119, 161101, doi: [10.1103/PhysRevLett.119.161101](https://doi.org/10.1103/PhysRevLett.119.161101)
- . 2017b, *The Astrophysical Journal Letters*, 848, L12, doi: [10.3847/2041-8213/aa91c9](https://doi.org/10.3847/2041-8213/aa91c9)
- . 2017c, *The Astrophysical Journal Letters*, 848, L13. <http://stacks.iop.org/2041-8205/848/i=2/a=L13>
- Abbott, B. P., Abbott, R., Abbott, T. D., et al. 2017, *Nature*, 551, 85, doi: [10.1038/nature24471](https://doi.org/10.1038/nature24471)
- Abbott, R., Abbott, T. D., Abraham, S., et al. 2021a, *The Astrophysical Journal Letters*, 915, L5, doi: [10.3847/2041-8213/ac082e](https://doi.org/10.3847/2041-8213/ac082e)
- Abbott, R., et al. 2021b. <https://arxiv.org/abs/2111.03606>
- Abbott et al. 2016, *Astrophys. J.*, 826, L13, doi: [10.3847/2041-8205/826/1/L13](https://doi.org/10.3847/2041-8205/826/1/L13)
- Aghanim, N., Akrami, Y., Ashdown, M., et al. 2020, *Astronomy & Astrophysics*, 641, A6, doi: [10.1051/0004-6361/201833910](https://doi.org/10.1051/0004-6361/201833910)
- Andres, N., et al. 2022, *Class. Quant. Grav.*, 39, 055002, doi: [10.1088/1361-6382/ac482a](https://doi.org/10.1088/1361-6382/ac482a)
- Annala, E., Gorda, T., Kurkela, A., & Vuorinen, A. 2018, *Phys. Rev. Lett.*, 120, 172703, doi: [10.1103/PhysRevLett.120.172703](https://doi.org/10.1103/PhysRevLett.120.172703)
- Ashton, G., Hübner, M., Lasky, P. D., et al. 2019, *ApJS*, 241, 27, doi: [10.3847/1538-4365/ab06fc](https://doi.org/10.3847/1538-4365/ab06fc)
- Aubin, F., et al. 2021, *Class. Quant. Grav.*, 38, 095004, doi: [10.1088/1361-6382/abe913](https://doi.org/10.1088/1361-6382/abe913)
- Bauswein, A., Just, O., Janka, H.-T., & Stergioulas, N. 2017, *ApJL*, 850, L34, doi: [10.3847/2041-8213/aa9994](https://doi.org/10.3847/2041-8213/aa9994)
- Bose, S., Pai, A., & Dhurandhar, S. V. 2000, *Int. J. Mod. Phys. D*, 9, 325, doi: [10.1142/S0218271800000360](https://doi.org/10.1142/S0218271800000360)
- Canizares, P., Field, S. E., Gair, J., et al. 2015, *Phys. Rev. Lett.*, 114, 071104, doi: [10.1103/PhysRevLett.114.071104](https://doi.org/10.1103/PhysRevLett.114.071104)
- Cannon, K., Hanna, C., & Peoples, J. 2015, *Likelihood-Ratio Ranking Statistic for Compact Binary Coalescence Candidates with Rate Estimation*. <https://arxiv.org/abs/1504.04632>
- Cannon, K., et al. 2012, *Astrophys. J.*, 748, 136, doi: [10.1088/0004-637X/748/2/136](https://doi.org/10.1088/0004-637X/748/2/136)
- Chabanat, E., Bonche, P., Haensel, P., Meyer, J., & Schaeffer, R. 1998, *NuPhA*, 635, 231, doi: [10.1016/S0375-9474\(98\)00180-8](https://doi.org/10.1016/S0375-9474(98)00180-8)
- Chatterjee, D., Ghosh, S., Brady, P. R., et al. 2020, *The Astrophysical Journal*, 896, 54, doi: [10.3847/1538-4357/ab8dbe](https://doi.org/10.3847/1538-4357/ab8dbe)
- Cho, M.-A. 2019, PhD thesis, University of Maryland
- Chornock et al. 2017, *The Astrophysical Journal Letters*, 848, L19. <http://stacks.iop.org/2041-8205/848/i=2/a=L19>
- Chu, Q., Kovalam, M., Wen, L., et al. 2021, *The SPIIR online coherent pipeline to search for gravitational waves from compact binary coalescences*. <https://arxiv.org/abs/2011.06787>
- Coughlin, M. W., Dietrich, T., Margalit, B., & Metzger, B. D. 2019a, *Monthly Notices of the Royal Astronomical Society: Letters*, 489, L91, doi: [10.1093/mnrasl/slz133](https://doi.org/10.1093/mnrasl/slz133)
- Coughlin, M. W., Dietrich, T., Doctor, Z., et al. 2018, *Monthly Notices of the Royal Astronomical Society*, 480, 3871, doi: [10.1093/mnras/sty2174](https://doi.org/10.1093/mnras/sty2174)
- Coughlin, M. W., Dietrich, T., Antier, S., et al. 2019b, *Monthly Notices of the Royal Astronomical Society*, 492, 863, doi: [10.1093/mnras/stz3457](https://doi.org/10.1093/mnras/stz3457)
- Coughlin, M. W., Dietrich, T., Heinzel, J., et al. 2020a, *Phys. Rev. Research*, 2, 022006, doi: [10.1103/PhysRevResearch.2.022006](https://doi.org/10.1103/PhysRevResearch.2.022006)
- Coughlin, M. W., Antier, S., Dietrich, T., et al. 2020b, *Nature Communications*, 11, 4129, doi: [10.1038/s41467-020-17998-5](https://doi.org/10.1038/s41467-020-17998-5)
- Coulter, D. A., Foley, R. J., Kilpatrick, C. D., et al. 2017, *Science*, 358, 1556, doi: [10.1126/science.aap9811](https://doi.org/10.1126/science.aap9811)
- Coulter et al. 2017, *Science*, 358, 1556, doi: [10.1126/science.aap9811](https://doi.org/10.1126/science.aap9811)
- Cowperthwaite, P. S., Berger, E., Villar, V. A., et al. 2017, *ApJL*, 848, L17, doi: [10.3847/2041-8213/aa8fc7](https://doi.org/10.3847/2041-8213/aa8fc7)
- Dal Canton, T., Nitz, A. H., Gadre, B., et al. 2021, *Astrophys. J.*, 923, 254, doi: [10.3847/1538-4357/ac2f9a](https://doi.org/10.3847/1538-4357/ac2f9a)
- Dent, T. 2023, *PyCBC Live p_{astro} for O4*, Tech. Rep. LIGO-T2300168, <https://dcc.ligo.org/T2300168/public>
- Dietrich, T., Coughlin, M. W., Pang, P. T. H., et al. 2020, *Science*, 370, 1450, doi: [10.1126/science.abb4317](https://doi.org/10.1126/science.abb4317)
- Drago, M., Klimenko, S., Lazzaro, C., et al. 2021, *SoftwareX*, 14, 100678
- Ewing, B., et al. 2023. <https://arxiv.org/abs/2305.05625>
- Farr, W. M., Gair, J. R., Mandel, I., & Cutler, C. 2015, *Phys. Rev. D*, 91, 023005, doi: [10.1103/PhysRevD.91.023005](https://doi.org/10.1103/PhysRevD.91.023005)
- Fernique, P., Boch, T., Donaldson, T., et al. 2014, *MOC - HEALPix Multi-Order Coverage map Version 1.0, IVOA Recommendation 02 June 2014*. <https://arxiv.org/abs/1505.02937>
- Fong, H. K. Y. 2018, *From simulations to signals: Analyzing gravitational waves from compact binary coalescences*
- Foucart, F., Hinderer, T., & Nissanke, S. 2018, *Phys. Rev. D*, 98, 081501, doi: [10.1103/PhysRevD.98.081501](https://doi.org/10.1103/PhysRevD.98.081501)
- Ghosh, S., Liu, X., Creighton, J., et al. 2021, *Physical Review D*, 104, doi: [10.1103/physrevd.104.083003](https://doi.org/10.1103/physrevd.104.083003)

- Goldstein, A., Veres, P., Burns, E., et al. 2017, *The Astrophysical Journal*, 848, L14, doi: [10.3847/2041-8213/aa8f41](https://doi.org/10.3847/2041-8213/aa8f41)
- Górski, K. M., Hivon, E., Banday, A. J., et al. 2005, *ApJ*, 622, 759, doi: [10.1086/427976](https://doi.org/10.1086/427976)
- Hannam, M., Schmidt, P., Bohé, A., et al. 2014, *Phys. Rev. Lett.*, 113, 151101, doi: [10.1103/PhysRevLett.113.151101](https://doi.org/10.1103/PhysRevLett.113.151101)
- Harry, I. W., & Fairhurst, S. 2011, *Physical Review D*, 83, doi: [10.1103/physrevd.83.084002](https://doi.org/10.1103/physrevd.83.084002)
- Hooper, S., Chung, S. K., Luan, J., et al. 2012, *Phys. Rev. D*, 86, 024012, doi: [10.1103/PhysRevD.86.024012](https://doi.org/10.1103/PhysRevD.86.024012)
- Hotokezaka, K., Nakar, E., Gottlieb, O., et al. 2018, <https://arxiv.org/abs/1806.10596>
- Husa, S., Khan, S., Hannam, M., et al. 2016, *Phys. Rev. D*, 93, 044006, doi: [10.1103/PhysRevD.93.044006](https://doi.org/10.1103/PhysRevD.93.044006)
- Huth, S., et al. 2022, *Nature*, 606, 276, doi: [10.1038/s41586-022-04750-w](https://doi.org/10.1038/s41586-022-04750-w)
- Kapadia, S. J., et al. 2020, *Class. Quant. Grav.*, 37, 045007, doi: [10.1088/1361-6382/ab5f2d](https://doi.org/10.1088/1361-6382/ab5f2d)
- Kasliwal, M. M., Kasen, D., Lau, R. M., et al. 2019, *Monthly Notices of the Royal Astronomical Society: Letters*, doi: [10.1093/mnras/lsz007](https://doi.org/10.1093/mnras/lsz007)
- Khan, S., Husa, S., Hannam, M., et al. 2016, *Phys. Rev. D*, 93, 044007, doi: [10.1103/PhysRevD.93.044007](https://doi.org/10.1103/PhysRevD.93.044007)
- Klimenko, S., Yakushin, I., Mercer, A., & Mitselmakher, G. 2008, *Classical and Quantum Gravity*, 25, 114029
- Klimenko, S., Vedovato, G., Drago, M., et al. 2011, *PhRvD*, 83, 102001, doi: [10.1103/PhysRevD.83.102001](https://doi.org/10.1103/PhysRevD.83.102001)
- Klimenko, S., et al. 2016, *Phys. Rev. D*, 93, 042004, doi: [10.1103/PhysRevD.93.042004](https://doi.org/10.1103/PhysRevD.93.042004)
- Kovalam, M., Patwary, M. A. K., Sreekumar, A. K., et al. 2022, *The Astrophysical Journal Letters*, 927, L9, doi: [10.3847/2041-8213/ac5687](https://doi.org/10.3847/2041-8213/ac5687)
- Lai, X., Zhou, E., & Xu, R. 2019, *The European Physical Journal A*, 55, 60, doi: [10.1140/epja/i2019-12720-8](https://doi.org/10.1140/epja/i2019-12720-8)
- Luan, J., Hooper, S., Wen, L., & Chen, Y. 2012, *Phys. Rev. D*, 85, 102002, doi: [10.1103/PhysRevD.85.102002](https://doi.org/10.1103/PhysRevD.85.102002)
- LV. 2019, *The Astrophysical Journal*, 875, 161, doi: [10.3847/1538-4357/ab0e8f](https://doi.org/10.3847/1538-4357/ab0e8f)
- LVK. 2018, *Physical Review Letters*, 121, doi: [10.1103/physrevlett.121.161101](https://doi.org/10.1103/physrevlett.121.161101)
- . 2021a, GWTC-3: Compact Binary Coalescences Observed by LIGO and Virgo During the Second Part of the Third Observing Run. <https://arxiv.org/abs/2111.03606>
- . 2021b, *Physical Review D*, 104, doi: [10.1103/physrevd.104.122004](https://doi.org/10.1103/physrevd.104.122004)
- . 2021c, *Physical Review D*, 104, doi: [10.1103/physrevd.104.102001](https://doi.org/10.1103/physrevd.104.102001)
- Lynch, R., Vitale, S., Essick, R., Katsavounidis, E., & Robinet, F. 2017, *Physical Review D*, 95, doi: [10.1103/physrevd.95.104046](https://doi.org/10.1103/physrevd.95.104046)
- Magee, R., Chatterjee, D., Singer, L. P., et al. 2021, *The Astrophysical Journal Letters*, 910, L21, doi: [10.3847/2041-8213/abed54](https://doi.org/10.3847/2041-8213/abed54)
- Margalit, B., & Metzger, B. 2017, *The Astrophysical Journal Letters*, 850, doi: [10.3847/2041-8213/aa991c](https://doi.org/10.3847/2041-8213/aa991c)
- Messick, C., et al. 2017, *Phys. Rev. D*, 95, 042001, doi: [10.1103/PhysRevD.95.042001](https://doi.org/10.1103/PhysRevD.95.042001)
- Mishra, T., et al. 2022, *Phys. Rev. D*, 105, 083018, doi: [10.1103/PhysRevD.105.083018](https://doi.org/10.1103/PhysRevD.105.083018)
- Morisaki, S., & Raymond, V. 2020, *Phys. Rev. D*, 102, 104020, doi: [10.1103/PhysRevD.102.104020](https://doi.org/10.1103/PhysRevD.102.104020)
- Morisaki, S., Smith, R., Tsukada, L., et al. 2023, <https://arxiv.org/abs/2307.13380>
- Most, E. R., Weih, L. R., Rezzolla, L., & Schaffner-Bielich, J. 2018, *Phys. Rev. Lett.*, 120, 261103, doi: [10.1103/PhysRevLett.120.261103](https://doi.org/10.1103/PhysRevLett.120.261103)
- Necula, V., Klimenko, S., & Mitselmakher, G. 2012, *J. Phys. Conf. Ser.*, 363, 012032, doi: [10.1088/1742-6596/363/1/012032](https://doi.org/10.1088/1742-6596/363/1/012032)
- Nitz, A. H., Dal Canton, T., Davis, D., & Reyes, S. 2018, *Phys. Rev. D*, 98, 024050, doi: [10.1103/PhysRevD.98.024050](https://doi.org/10.1103/PhysRevD.98.024050)
- Nitz, A. H., Dent, T., Dal Canton, T., Fairhurst, S., & Brown, D. A. 2017, *Astrophys. J.*, 849, 118, doi: [10.3847/1538-4357/aa8f50](https://doi.org/10.3847/1538-4357/aa8f50)
- Nitz, A. H., Schäfer, M., & Dal Canton, T. 2020, *Astrophys. J. Lett.*, 902, L29, doi: [10.3847/2041-8213/abbc10](https://doi.org/10.3847/2041-8213/abbc10)
- Pian et al. 2017, *Nature*, 551, 67 EP. <http://dx.doi.org/10.1038/nature24298>
- Piotrkowski, B. J. 2022
- Pratten, G., et al. 2021, *Phys. Rev. D*, 103, 104056, doi: [10.1103/PhysRevD.103.104056](https://doi.org/10.1103/PhysRevD.103.104056)
- Radice, D., Perego, A., Zappa, F., & Bernuzzi, S. 2018, *The Astrophysical Journal Letters*, 852, L29, <http://stacks.iop.org/2041-8205/852/i=2/a=L29>
- Robinet, F., Arnaud, N., Leroy, N., et al. 2020, *SoftwareX*, 12, 100620, doi: [10.1016/j.softx.2020.100620](https://doi.org/10.1016/j.softx.2020.100620)
- Romero-Shaw, I. M., et al. 2020, *Mon. Not. Roy. Astron. Soc.*, 499, 3295, doi: [10.1093/mnras/staa2850](https://doi.org/10.1093/mnras/staa2850)
- Rosswog, S., Feindt, U., Korobkin, O., et al. 2017, *Class. Quant. Grav.*, 34, 104001, doi: [10.1088/1361-6382/aa68a9](https://doi.org/10.1088/1361-6382/aa68a9)
- Roy, S., Sengupta, A. S., & Ajith, P. 2019, *Phys. Rev. D*, 99, 024048, doi: [10.1103/PhysRevD.99.024048](https://doi.org/10.1103/PhysRevD.99.024048)
- Roy, S., Sengupta, A. S., & Thakor, N. 2017, *Phys. Rev. D*, 95, 104045, doi: [10.1103/PhysRevD.95.104045](https://doi.org/10.1103/PhysRevD.95.104045)

- Sachdev, S., Magee, R., Hanna, C., et al. 2020, The Astrophysical Journal Letters, 905, L25, doi: [10.3847/2041-8213/abc753](https://doi.org/10.3847/2041-8213/abc753)
- Sakon, S., et al. 2022, Template bank for compact binary mergers in the fourth observing run of Advanced LIGO, Advanced Virgo, and KAGRA. <https://arxiv.org/abs/2211.16674>
- Savchenko, V., Ferrigno, C., Kuulkers, E., et al. 2017, The Astrophysical Journal, 848, L15, doi: [10.3847/2041-8213/aa8f94](https://doi.org/10.3847/2041-8213/aa8f94)
- Shibata, M., & Hotokezaka, K. 2019, Annual Review of Nuclear and Particle Science, 69, 41, doi: [10.1146/annurev-nucl-101918-023625](https://doi.org/10.1146/annurev-nucl-101918-023625)
- Singer, L., & Racusin, J. 2023, Bulletin of the AAS, 55
- Singer, L. P., & Price, L. R. 2016, PhRvD, 93, 024013, doi: [10.1103/PhysRevD.93.024013](https://doi.org/10.1103/PhysRevD.93.024013)
- Smartt et al. 2017, Nature, 551, 75 EP . <http://dx.doi.org/10.1038/nature24303>
- Smith, R., Field, S. E., Blackburn, K., et al. 2016, Phys. Rev., D94, 044031, doi: [10.1103/PhysRevD.94.044031](https://doi.org/10.1103/PhysRevD.94.044031)
- Speagle, J. S. 2020, Mon. Not. Roy. Astron. Soc., 493, 3132, doi: [10.1093/mnras/staa278](https://doi.org/10.1093/mnras/staa278)
- Szczepańczyk, M. J., et al. 2023, Phys. Rev. D, 107, 062002, doi: [10.1103/PhysRevD.107.062002](https://doi.org/10.1103/PhysRevD.107.062002)
- Tsukada, L., et al. 2023. <https://arxiv.org/abs/2305.06286>
- Urban, A. L. 2016, PhD thesis, University of Wisconsin-Milwaukee
- Usman, S. A., Nitz, A. H., Harry, I. W., et al. 2016, Classical and Quantum Gravity, 33, 215004, doi: [10.1088/0264-9381/33/21/215004](https://doi.org/10.1088/0264-9381/33/21/215004)
- Villa-Ortega, V., Dent, T., & Barroso, A. C. 2022, Astrophysical Source Classification and Distance Estimation for PyCBC Live. <https://arxiv.org/abs/2203.10080>
- Watson, D., Hansen, C. J., Selsing, J., et al. 2019, Nature, 574, 497, doi: [10.1038/s41586-019-1676-3](https://doi.org/10.1038/s41586-019-1676-3)
- Wen, L. 2008, International Journal of Modern Physics D, 17, 1095, doi: [10.1142/s0218271808012723](https://doi.org/10.1142/s0218271808012723)